nature communications

Article

https://doi.org/10.1038/s41467-025-66339-x

Strong yet superelastic ceramic aerogel enabled by synergistic soft-hard inter-nanowire nodes

Received: 5 December 2024

Accepted: 4 November 2025

Published online: 21 November 2025

Check for updates

De Lu[1], Lei Su[2] ✉, Lei Zhuang[2], Min Niu[2], Kang Peng[2], Pengcheng Zhang[2], Xiaowu Wang[2], Zhentao Ni[2], Shuhai Jia[3] & Hongjie Wang[2] ✉

Elastic ceramic aerogels have drawn broad attention for use in aerospace, energy storage, and thermal protection systems, where lightweight structures with thermal stability and mechanical robustness are required. Yet their practical application is often limited by insufficient strength. Achieving both high strength and high elasticity in ceramic nanowire aerogels remains challenging because these properties are typically mutually constrained. Here we design silicon carbide nanowire aerogels reinforced by dual-phase nodes composed of pyrolytic carbon (PyC) and amorphous silica (SiO_2) to resolve this conflict. Experimental measurements together with large-scale atomic/molecular massively parallel simulator (LAMMPS) and finite element simulations show that amorphous SiO_2 improves load-bearing efficiency by distributing stress uniformly, while PyC relieves local stress concentrations and prevents premature SiO_2 fracture, producing a clear synergistic effect. The resulting aerogels exhibit a compressive strength of 10.9 MPa at 80% strain and a resilience of about 90%. This dual-phase strategy provides an effective route to tailor the mechanical response of ceramic aerogels and expand their use in extreme environments such as high temperature, low oxygen, and vacuum conditions, where strength, elasticity, and long-term reliability are required.

Ceramic aerogels are valued for their ultralow density, high thermal stability, and chemical inertness, making them highly desirable for demanding applications in aerospace, energy storage, and thermal insulation[1–6]. In service, however, these materials are often subjected to complex and dynamic stress states that place strict requirements on mechanical reliability[7]. Although ceramic aerogels possess many advantages, they generally remain brittle and weak, which limits their ability to sustain high loads. To enhance their mechanical performance, including compressive resilience, bendability, and stretchability, recent studies have emphasized multiscale structural design and compositional optimization[8–10]. For instance, constructing porous cellular, random nest-like, or lamellar architectures with tunable bond angles and fewer micro-defects has enabled amorphous oxide nanofiber-based aerogels to achieve substantial compressive recovery even under large strains of up to 80%[11–16]. Despite these advances, most ceramic aerogels still exhibit relatively low strength, with maximum compressive stresses typically between several kPa and a few hundred kPa, far below the levels required for aerospace thermal protection or other dynamically loaded systems. Introducing anisotropic honeycomb architectures can improve strength along preferred directions[17,18], but usually at the expense of resilience. Likewise, increasing the degree of nanowire cross-linking enhances strength yet reduces recoverability[19,20]. These trade-offs highlight the persistent challenge of combining high strength with high resilience in ceramic aerogels.

[1]State Key Laboratory of Porous Metal Materials, Xi'an Jiaotong University, Xi'an, China. [2]State Key Laboratory for Mechanical Behavior of Materials, Xi'an Jiaotong University, Xi'an, China. [3]School of Mechanical Engineering, Xi'an Jiaotong University, Xi'an, China. ✉e-mail: lei.su@xjtu.edu.cn; hjwang@xjtu.edu.cn

Nature offers valuable insights into achieving diverse mechanical properties using limited material systems[21]. For example, the regulation of mechanical behavior in the actin cytoskeleton through F-actin and cross-linking proteins has inspired many material design strategies[22]. In the actin cytoskeleton, crosslinking density is a key factor that enhances strength and stiffness, while the compliance of the crosslinkers governs stress redistribution within the network. Drawing inspiration from this concept, our previous work showed that the mechanical behavior of nanowire aerogels is largely determined by the type of nodes connecting the nanowires and the coatings on their surfaces. For instance, introducing pyrolytic carbon (PyC) nodes or coatings markedly improved the elastic recovery of nanowire aerogels[23], whereas silicon carbide (SiC) nodes or coatings led to pseudoplastic behavior accompanied by a near-complete loss of compressive elastic recovery[24]. This contrast arises from the different deformation constraints imposed by the two materials. SiC, with strong covalent bonds and high intrinsic stiffness, restricts nanowire deformation and produces a rigid network that limits elastic recovery. In comparison, PyC consists of locally ordered graphene-like layers held together by van der Waals forces, with additional sp^3 cross-linking that maintains structural stability[25]. This configuration allows PyC to deform more readily than SiC, accommodating moderate nanowire motion and reducing stress concentration at the nodes. Consequently, PyC behaves as a soft node relative to SiC, promoting greater recoverability of the nanowire framework. These observations indicate that the composition of nodes and coatings is crucial for controlling the mechanical response of nanowire aerogels. Achieving both high strength and high elasticity requires an optimal level of constraint imposed by the nodes and coatings on nanowire deformation: excessive constraint suppresses recoverability, whereas insufficient constraint weakens strength.

Here we present a strategy to overcome the conventional trade-off between strength and elasticity in ceramic aerogels by constructing synergistic soft–hard inter-nanowire nodes within SiC nanowire networks. The nodes have a dual-phase configuration composed of stiff amorphous silica (SiO_2) and compliant PyC. During compression, PyC deforms readily and stores mechanical energy, while SiO_2 with its higher modulus, provides structural reinforcement and improves load-bearing efficiency. At the same time, PyC mitigates stress concentration around SiO_2 regions, delaying the onset of fracture under large compressive strains. Through this design, we achieved a ceramic aerogel that combines superelasticity with high strength, reaching a maximum compressive recovery strain of 80% and a peak stress of 10.9 MPa, among the highest values reported for elastic ceramic aerogels. This design concept provides a new route for regulating the mechanical behavior of ceramic aerogels.

Results and discussion

Design and fabrication of HC-SiC@(SiO_2/PyC) nanowire aerogels (NWAs)

SiC nanowire aerogels with an initial density of 10 mg·cm^{-3} were used as the starting matrix. The crosslinking density between nanowires was increased by a hot-pressing process. By adjusting the applied pressure, the density of the resulting highly cross-linked SiC nanowire aerogels (HC-SiC NWAs) could be tuned, allowing control over the degree of inter-nanowire bonding. Unless otherwise specified, the HC-SiC NWA described hereafter refers to a sample with a density of 100 mg·cm^{-3}. Scanning electron microscopy (SEM) revealed that hot pressing significantly increased the interconnection between nanowires (Supplementary Fig. 1). Subsequent oxidation at 1000 °C for 1 h produced an amorphous SiO_2 layer on the surface of SiC nanowires, forming SiO_2 nodes between adjacent nanowires (donated as HC-SiC@SiO_2 NWA, Supplementary Fig. 2). PyC was then introduced by chemical vapor infiltration (CVI), coating the SiO_2 surface and generating SiO_2/PyC dual-component junctions (denoted as HC-SiC@(SiO_2/PyC) NWA, Fig. 1a). When the CVI process was applied directly to unoxidized nanowires, PyC coatings were deposited on the SiC surface, resulting in aerogels with PyC junctions (denoted as HC-SiC@PyC NWA, Supplementary Fig. 3). For nanowires with dual coatings, transmission electron microscopy (TEM) and corresponding energy-dispersive spectroscopy (EDS) maps confirmed a SiO_2 layer about 28 nm thick surrounding each SiC nanowire, followed by an outer PyC layer of similar thickness (Fig. 1b–d). High-resolution TEM further revealed intimate adhesion among the PyC layer, the SiO_2 coating, and the SiC core (Fig. 1e).

Mechanical properties

Significant differences in mechanical behavior were observed among nanowire aerogels with different node compositions and surface coatings. The HC-SiC@PyC NWA (121 mg cm^{-3}) exhibited the highest compressive recoverability, maintaining 91% resilience under 80% strain (Fig. 2a), but showed the lowest strength and modulus, with a maximum stress of 1.1 MPa. The HC-SiC@SiO_2 NWA (110 mg cm^{-3}) displayed a fivefold increase in strength and a twofold increase in modulus at the same strain level, whereas its compressive recovery decreased to 40% (Fig. 2b). In this sample, the stress rose sharply between 60% and 80% strain, suggesting pronounced densification of the nanowire network. SEM observations confirmed that this process was accompanied by extensive nanowire fracture (Supplementary Fig. 4). The high strength but poor resilience of the HC-SiC@ SiO_2 aerogel result from the brittleness and limited deformability of the SiO_2 junctions. In comparison, the stress evolution in the PyC-containing aerogel was more gradual, consistent with a more compliant deformation behavior.

Notably, HC-SiC@(SiO_2/PyC) NWA (143 mg cm^{-3}) exhibited both high strength and excellent resilience (Fig. 2c). Its maximum stress reached 10.9 MPa, which is about 60% higher than that of the HC-SiC@SiO_2 NWA (6.8 MPa) and nearly an order of magnitude greater than that of the HC-SiC@PyC NWA (1.1 MPa) (Fig. 2d). The compressive modulus also increased to 5.5 MPa, compared with 4.2 MPa for HC-SiC@SiO_2 and 0.7 MPa for HC-SiC@PyC (Fig. 2e and Supplementary Table 1). This enhancement in stiffness arises from two factors. First, the SiO_2/PyC dual-layer nodes were formed by depositing an additional PyC layer on the existing SiO_2 coating, producing thicker SiC@(SiO_2/PyC) nanowires as the fundamental structural elements. The increased cross-sectional area improves the rigidity of the framework. Second, the compliant PyC layer reduces local stress concentration at the brittle SiO_2 nodes, increasing their load-bearing capacity and contributing to a stiffer overall response. Despite the substantial gains in strength and stiffness, the HC-SiC@(SiO_2/PyC) NWA maintained excellent recoverability, with a recovery ratio of about 90% at 80% strain, much higher than the 40% observed in HC-SiC@SiO_2 and comparable to the 91% of HC-SiC@PyC (Fig. 2c).

At a strain of 5%, the HC-SiC@(SiO_2/PyC) NWA exhibited the lowest loss factor (0.04), compared with 0.25 for HC-SiC@SiO_2 and 0.29 for HC-SiC@PyC. This behavior arises from the mechanical robustness of the soft–hard dual nodes, which effectively suppress structural damage during deformation. After 1000 compression cycles at 60% strain, the permanent deformation remained as low as about 9%, confirming excellent fatigue resistance and structural stability (Supplementary Fig. 5). The influence of crosslinking density on mechanical performance was also examined (Supplementary Fig. 6). As the crosslinking density and, consequently, the aerogel density increased, the restriction on nanowire deformation became stronger, leading to a marked improvement in load-bearing capacity. At small strains (for example, 5%), the increased number of nodes enhanced load transfer efficiency across the network (Supplementary Fig. 7), reducing sliding and friction between nanowires and thereby lowering the energy dissipation coefficient. At high compressive strains above 60%, however, the greater constraint imposed by the dense nodes

https://doi.org/10.1038/s41467-025-66339-x

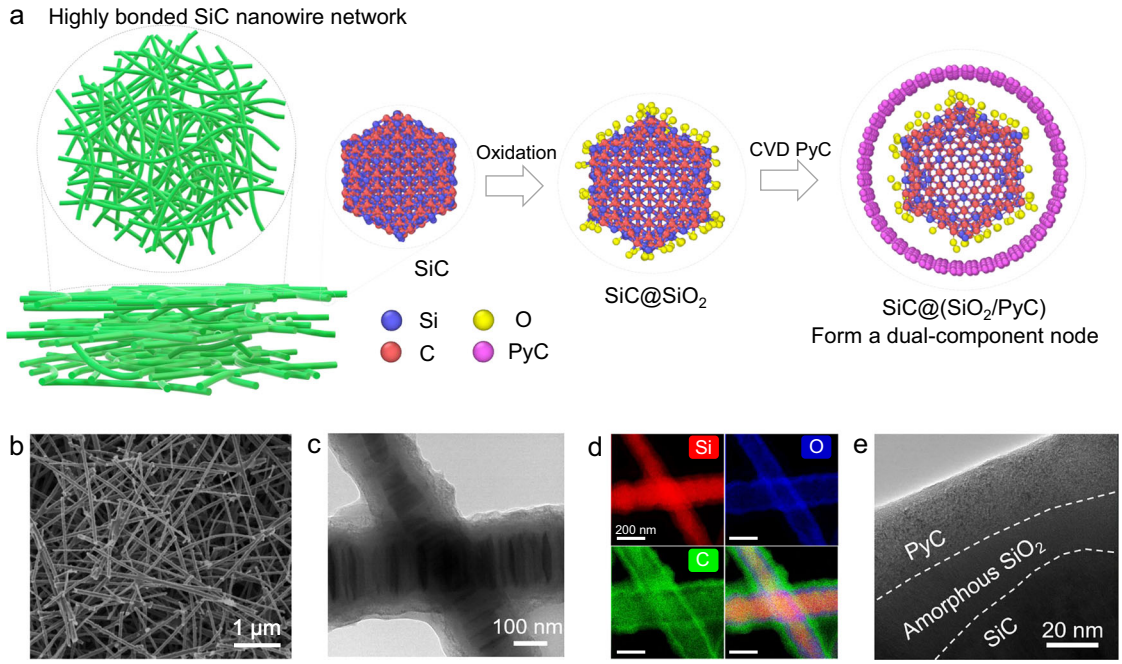

Fig. 1 | Schematic illustration of the design and the microstructure characteristics of highly crosslinked nanowire aerogels with dual-phase nodes design. **a** Design of a highly cross-linked layered ceramic nanowire aerogel with "soft-hard" dual phase nodes. **b** SEM images of aerogel depicting the highly cross-linked characteristics of nanowires within the aerogel (representative of three independent samples, $n = 3$). **c** TEM image of two inter-bonded nanowires, and **d** the corresponding EDS elemental mapping of Si, O, and C (representative of three independent measurements, $n = 3$). The red, blue, and green contrasts correspond to Si, O, and C signals, respectively; alternative color schemes yield identical elemental distributions. Scale bars, 200 nm. **e** High-resolution TEM image revealing the dual-phase SiO_2/PyC coating on the surface of the SiC nanowire (representative of three independent observations, $n = 3$).

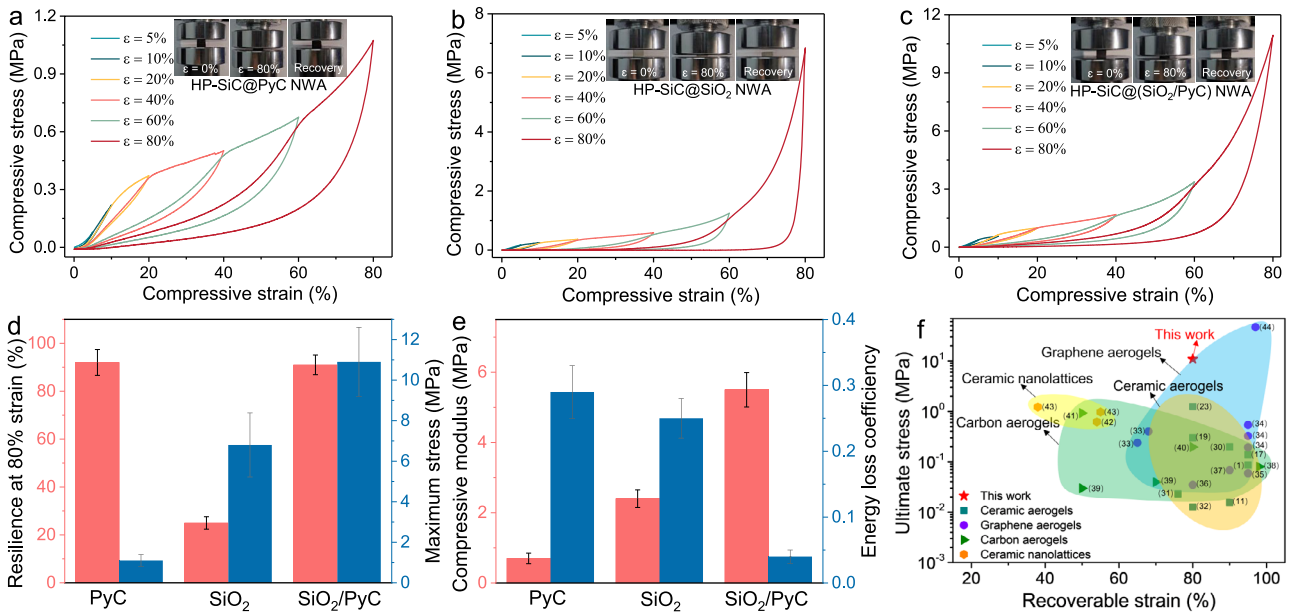

Fig. 2 | Mechanical behavior of nanowire aerogels with different nodes. Compressive stress versus strain curves of **a** HC-SiC@PyC NWA, **b** HC-SiC@SiO_2 NWA, **c** HC-SiC@(SiO_2/PyC) NWA. Insets show opitcal images of the samples during the compression-recovery process. **d** Resilience at 80% strain and the maximum of aerogels with different nodes. **e** Compressive modulus and energy loss coefficiency aerogels with different nodes. **f** Ashby plot of ultimate stress versus maximum recoverable strain for resilient inorganic aerogels[1,11,17,19,23,30–44]. Source data are provided as a Source Data file.

made individual nanowires more prone to fracture. This damage degraded the structural integrity of the three-dimensional framework, ultimately reducing the compressive recoverability of the aerogel.

The combination of high strength, high modulus and high resilience endows HC-SiC@(SiO_2/PyC) NWA with a significant strength advantage over other highly elastic ceramic aerogels, making their performance comparable to that of high-performance nanotube or graphene aerogels (Fig. 2f). When normalized by density, this material shows the highest specific modulus among the three types, demonstrating superior stiffness-to-weight efficiency enabled by the dual-

phase junction design. As summarized in Supplementary Table 2, both the stiffness and specific modulus of the HC-SiC@(SiO_2/PyC) NWA exceed those of most previously reported superelastic ceramic, carbon-based, and graphene aerogels, confirming the effectiveness of the dual-phase node structure in overcoming the trade-off between strength and elasticity. The HC-SiC@(SiO_2/PyC) NWA also exhibits low thermal conductivity of about 0.0382 $W{\cdot}m^{-1}{\cdot}K^{-1}$ at room temperature, comparable to leading insulating materials. It maintains excellent thermal stability: after annealing at 1500 °C for 2 h in Ar, the microstructure remains intact, and the aerogel retains approximately 90% of its original compressive recoverability and 84% of its initial strength (9.2 MPa), with the modulus remains at about 87% of its pre-annealing value (Supplementary Fig. 8). These combined properties, including high strength, resilience, fatigue resistance, ultralow thermal conductivity, and thermal stability, make the HC-SiC@(SiO_2/PyC) NWA a promising candidate material for thermal protection systems, vibration-damping structural insulators, and high-temperature aerospace components where both mechanical robustness and energy efficiency are required.

Strengthening and elastic deformation mechanism

To elucidate how different nodes or coatings influence the mechanical response of ceramic nanowire aerogels, we conducted multiscale simulations combining molecular dynamics (MD) of individual nanowires with finite element modeling of 3D nanowire networks. The von Mises stress and atomic shear strain maps from LAMMPS simulations reveal clear distinctions among the SiC@SiO_2, SiC@PyC, and SiC@(SiO_2/PyC) models. In the SiC@SiO_2 model (Fig. 3a), the SiC core experiences high von Mises stress with a markedly non-uniform distribution, revealing localized stress concentrations. Compared with the pristine SiC nanowire, the overall stress level is lower (Supplementary Fig. 9), indicating that even a thin SiO_2 shell can partially relieve stress during bending. The shear strain within the SiC core is also unevenly distributed (Supplementary Fig. 10), indicating that although the SiO_2 shell transfers load effectively, the concentrated deformation in the core increases the likelihood of brittle failure. By contrast, the SiC@PyC nanowire shows lower and more uniform stress within the SiC core, whereas the PyC coating bears higher but evenly distributed stress. The corresponding shear strain distribution is also the lowest and most homogeneous among the three models. These results indicate that the PyC coating can absorb and redistribute deformation, protecting the SiC core and suppressing local failure. The deformability of PyC arises from its locally ordered layered structure, where graphene fragments accommodate deformation via interlayer sliding, curling, and nanoscale buckling of the turbostratic layers[26,27]. This structural flexibility, however, also limits the load-bearing contribution of the SiC core.

In the SiC@(SiO_2/PyC) model, the SiC core shows higher average stress and shear strain than in SiC@PyC, but both are more uniformly distributed than in SiC@SiO_2. The SiO_2 and PyC layers also bear substantial and well-distributed stress, showing that the dual-layer architecture promotes cooperative load sharing. The higher and more homogeneous shear strain in the SiC core indicates that the dual coating not only suppresses local failure but also activates the load-bearing capacity of the core more effectively. The outer PyC layer accommodates most of the deformation while relieving stress concentrations in the SiO_2 layer, preventing its premature fracture. Meanwhile, the stiffer SiO_2 layer constrains the deformation of the SiC nanowire, enhancing the overall load-bearing capability of the network. This interplay allows the dual-layer structure to combine the flexibility of PyC with the rigidity of SiO_2, maintaining strain adaptability while improving structural strength. It should be noted that the nanowires used in the MD simulations are considerably smaller than those in experiments due to computational limitations. Although the absolute values differ, the simulations provide qualitative insight into how coating composition governs the deformation behavior of the nanowires.

The three-dimensional finite element results further corroborate the experimental and atomistic observations. Under 50% compressive strain (Fig. 3b), the HP-SiC@SiO_2 network shows extensive stress concentration in both the SiC core and the stiff SiO_2 shell, indicating a limited ability to redistribute load and accommodate deformation. By contrast, the HP-SiC@PyC network experiences lower stresses within the compliant PyC coating, and stress localization occurs mainly at the inter-nanowire junctions, implying slower stress transfer through the network. The HP-SiC@(SiO_2/PyC) structure, however, achieves a more uniform stress distribution across all components (SiC, SiO_2, and PyC), reflecting improved load transfer efficiency enabled by the soft–hard dual-layer coating. The evolution of stress with increasing strain further reveals differences in load transfer behavior. In the HP-SiC@(SiO_2/PyC) network, a continuous load-bearing framework forms at about 7% strain, demonstrating the fastest establishment of global stress-transfer. This feature aligns with its experimentally observed low energy-loss coefficient and high recovery ratio. In comparison, the HP-SiC@SiO_2 and HP-SiC@PyC networks require approximately 12% and 21% strain, respectively, to achieve similar stress percolation, indicating lower structural responsiveness and greater energy dissipation.

Upon unloading (Fig. 3c), the HP-SiC@(SiO_2/PyC) network exhibited the highest structural recoverability with minimal permanent deformation. The HP-SiC@PyC network showed moderate recovery, whereas the HP-SiC@SiO_2 structure retained considerable residual deformation, indicating limited strain accommodation. These results demonstrate the advantage of the dual-layer junction architecture in promoting both recoverable deformation and structural stability. Representative force–displacement curves from the simulations (Supplementary Fig. 11) illustrate the effect of node configuration on network mechanics. The HP-SiC@SiO_2 aerogel shows pronounced load fluctuations, suggesting frequent local instabilities or damage events during compression, most likely caused by stress concentration and brittle fracture at the rigid SiO_2 junctions. In contrast, the HP-SiC@(SiO_2/PyC) aerogel exhibits smaller fluctuation amplitudes and a much higher peak load, reflecting enhanced load-bearing capacity and improved structural continuity provided by the synergistic soft–hard dual-layer nodes. The HP-SiC@PyC aerogel displays the smoothest curve, corresponding to stable yet lower load-bearing performance, consistent with its more compliant mechanical behavior. The FEM simulations were carried out using idealized linear-elastic models under simplified boundary conditions. Although the computed stress and force values are not intended to represent exact experimental magnitudes, the simulations provide qualitative insight into the differences in stress distribution and damage evolution among networks with distinct node architectures.

Combined with the MD simulations, these results reveal a clear synergistic interaction between the stiff SiO_2 and the compliant PyC components. The PyC coating, with its partially ordered layered structure that allows local sliding and curvature, buffers strain and relieves stress concentration near the brittle nodes. In parallel, the SiO_2 layer efficiently transmits load throughout the network, enhancing its overall stiffness. The cooperation of the two layers enables coordinated deformation and robust load transfer, producing a well-balanced combination of strength and elasticity that exceeds the capability of either component alone.

Dynamic mechanical performances

In practical applications such as dynamic thermal sealing, vibration damping, and environments involving complex stress conditions, as commonly found in aerospace, automotive, and other high-performance engineering systems, materials are frequently subjected

https://doi.org/10.1038/s41467-025-66339-x

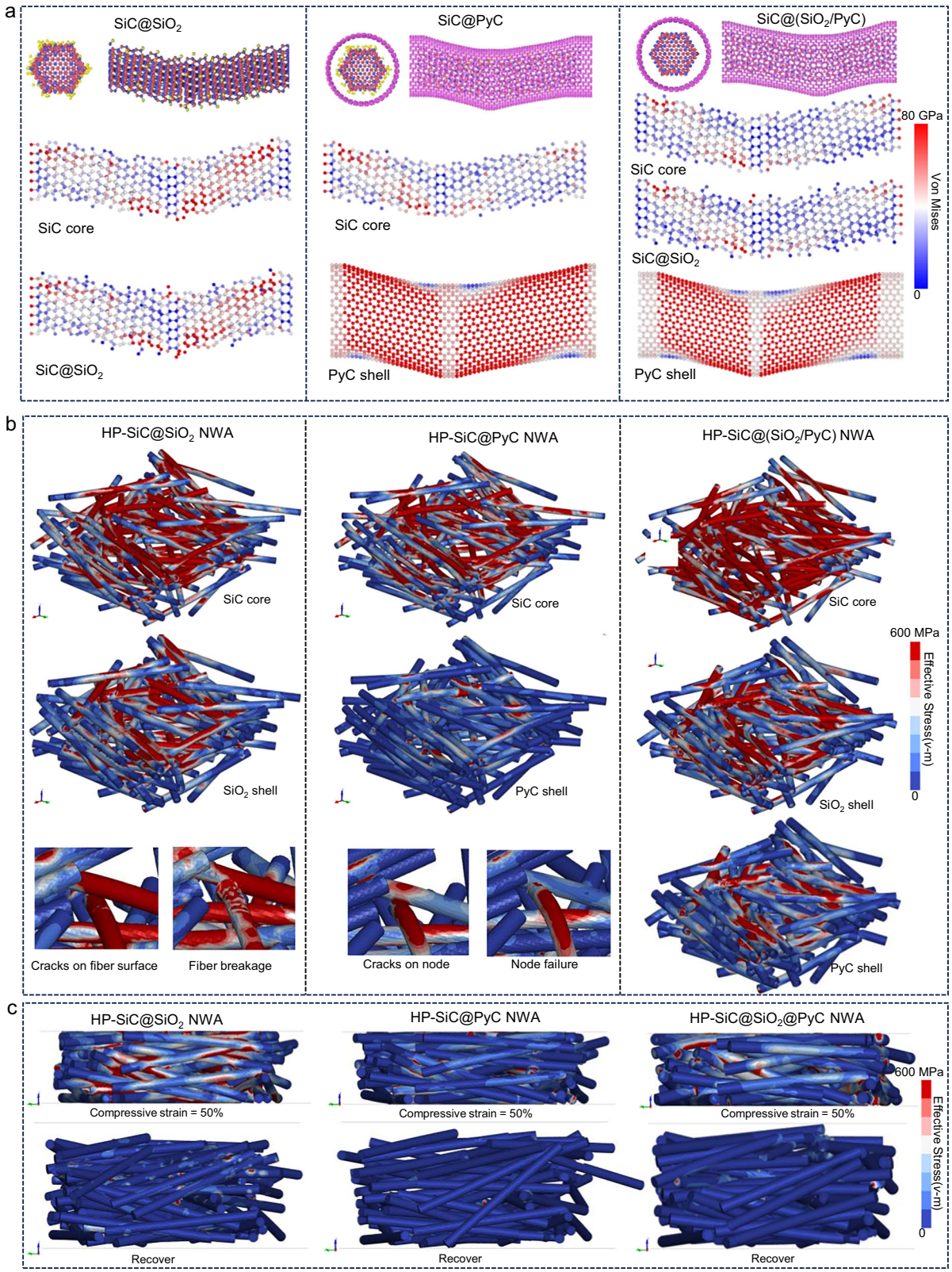

Fig. 3 | Stress distribution and deformation behaviours of nanowires and nanowire aerogels with different node designs. a Von Mises stress contour plots of the cross-section of single nanowires under bending with different coatings simulated using LAMMPS. **b** Finite element simulations showing the von Mises stress distribution in nanowire aerogels with different nodes/coatings under 50% compressive strain. Clear differences in stress localization and distribution patterns are observed among the three designs. **c** Evolution of von Mises stress in side-view cross-sections of the three nanowire networks during compression and unloading. The SiO_2/PyC node design shows more uniform stress distribution and better structural recoverability compared to the SiO_2 or PyC node designs.

to fluctuating stress and strain across a wide range of frequencies and temperatures. For aerogels, characterized by ultralow density and high porosity, such dynamic loads pose substantial challenges to structural stability. Dynamic mechanical analysis (DMA) provides a comprehensive evaluation of the frequency- and temperature-dependent viscoelastic behavior of aerogels, offering valuable insight into their reliability under service conditions. DMA tests show that the viscoelastic properties of the nanowire aerogels remain stable over a broad frequency range (0.1–80 Hz, Fig. 4a–c) and temperature window (−120 °C to 300 °C, Fig. 4d–e and Supplementary Fig. 12) under a fixed oscillatory strain amplitude of ±2%. Distinct differences are observed among the three types of aerogels. The HC-SiC@(SiO_2/PyC) NWA exhibits the highest storage modulus, followed by HC-SiC@SiO_2, while HC-SiC@PyC shows the lowest value (Fig. 4a). This behavior indicates that the dual-layer junctions combine the stiffness of SiO_2, which promotes elastic energy storage, with the flexibility of PyC, which facilitates strain accommodation. The cooperation of these two components yields an optimized balance between load transfer and energy retention. The loss modulus displays the opposite trend (Fig. 4b): HC-SiC@PyC shows the highest loss modulus, corresponding to greater energy dissipation arising from the pronounced deformability of PyC, whereas HC-SiC@(SiO_2/PyC) shows the lowest value, and HC-SiC@SiO_2 lies in between. Although PyC generally enhances damping, the presence of SiO_2 in the dual-layer nodes constrains its deformation and lowers the overall energy loss (Fig. 4c). This interaction reduces the flexibility of PyC, resulting in lower viscoelastic damping in the dual-layer structure. Furthermore, at a fixed frequency of 20 Hz, the viscoelastic behavior of HC-SiC@(SiO_2/PyC) remains nearly insensitive to temperature variations in the range of −120 °C to 300 °C (Fig. 4d, e). Fatigue tests performed at 50 Hz further demonstrate the durability of the nanowire aerogels. The viscoelastic properties remain stable after 100,000 loading cycles at ±2% strain (Fig. 4f), confirming the excellent elasticity and fatigue resistance of the HC-SiC@(SiO_2/PyC) NWA.

These results are consistent with the LAMMPS and finite element simulations, which showed that PyC mitigates stress concentration through its ability to deform, whereas SiO_2 increases structural rigidity and promotes efficient load transfer. The dual-layer nodes integrate the advantages of both components, producing a nanowire network that combines high strength with pronounced elasticity and achieves an effective balance between energy storage and dissipation. The cooperative interaction between the soft PyC and the stiff SiO_2 ultimately imparts superior mechanical robustness and resilience to the ceramic nanowire aerogels.

In summary, we have demonstrated that dual nodes composed of amorphous SiO_2 and PyC markedly improve the mechanical properties of ceramic nanowire aerogels. The cooperative interaction between the two components enables an exceptional balance between strength and elasticity. The SiO_2 layer enhances load-bearing capacity by efficiently transferring stress, whereas the PyC layer mitigates stress concentration and protects the SiO_2 from early fracture. As a result, the nanowire aerogels exhibit a compressive strength of 10.9 MPa at 80% strain and recover up to 90% of their original height after unloading. This study provides a general strategy for overcoming the conventional trade-off between strength and elasticity in ceramic nanowire aerogels by optimizing the mechanical characteristics of inter-nanowire nodes, paving the way for the rational design of ceramic nanowire aerogels with tunable mechanical properties for diverse advanced applications.

Methods

Preparation of SiC NWAs

A siloxane sol was prepared by mixing methyltrimethoxysilane (80 × *g*), dimethyldimethoxysilane (20 × *g*), ethanol (200 × *g*), and deionized water (40 × *g*), followed by mechanical stirring for 30 min[28]. By adjusting the hot-pressing pressure, the desired density of the HC-SiC NWA was achieved. Short-cut carbon fibers (40 × *g*, TZ40, average diameter ~7 μm, length 1–2 mm) were gradually added and dispersed at 1000 rpm for 20–30 min. The mixture was then vacuum-filtered to remove excess liquid, forming a porous green body, which was subsequently cured at 100 °C for 5 h.

The cured samples were heated to 1550 °C at a ramp rate of 5 °C min^{-1} under a 0.2 MPa argon atmosphere and maintained at that temperature for 2 h. During this step, entangled SiC nanowires formed

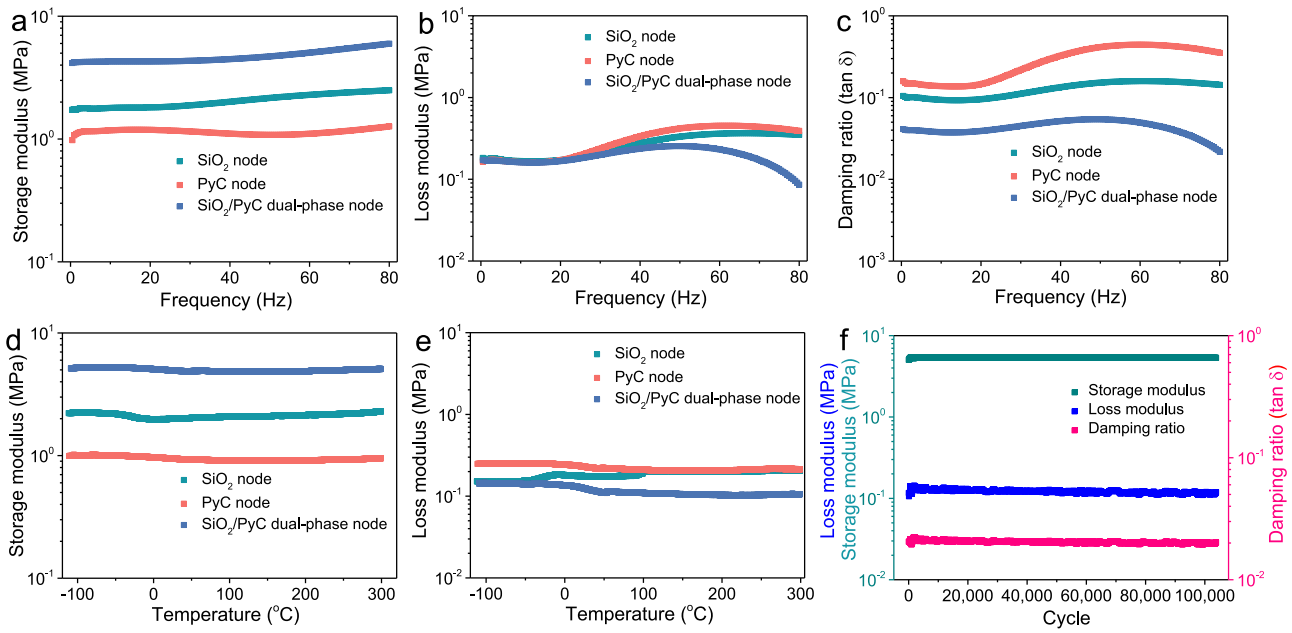

Fig. 4 | The effect of nodes types on the viscoelasticity of aerogels. a–c Storage modulus, loss modulus, and damping ratio of the nanowire aerogel as function of frequency (0.1–100 Hz) at room temperature. **d**, **e** Temperature dependence (−120 °C–300 °C) of the storage modulus, loss modulus of the nanowire aerogel at a constant frequency of 20 Hz. **f** Fatigue resistance of the nanowire aerogels with dual nodes (with an oscillatory strain of 2%, 50 Hz, 10^5 cycles). Source data are provided as a Source Data file.

via in-situ reactions, including:

$$SiO(g) + 2C(s) \rightarrow SiC(s) + CO(g)$$

$$SiO2(s) + 3C(s) \rightarrow SiC(s) + 2CO(g)$$

$$SiO(g) + 3CO(g) \rightarrow SiC(s) + 2CO_2(g)$$

Finally, the SiC nanowire/carbon fiber composites were heat-treated in air at 700 °C for 3 h to remove the carbon fibers, resulting in freestanding SiC nanowire aerogels with a density of approximately 10 mg cm^{-3}.

Preparation of HC-SiC NWAs

Pristine SiC NWAs with an initial density of 10 mg cm^{-3} were subjected to hot pressing at 1300 °C for 2 h under an argon atmosphere. Pressures of 0.5, 1.0, and 2.0 MPa were applied to obtain aerogels with final densities of approximately 50, 100, and 200 mg cm^{-3}, respectively. The increased crosslinking density between nanowires in these samples was confirmed by SEM observations.

Formation of SiO_2 nodes

To introduce SiO_2 coatings and inter-nanowire nodes, the HC-SiC NWAs were oxidized in ambient air at 1000 °C for 1 h using a muffle furnace. The heating rate was set to 10 °C min^{-1}. During this process, an amorphous SiO_2 layer formed on the surfaces of the SiC nanowires, and adjacent nanowires were locally fused by the SiO_2 phase, resulting in the formation of rigid SiO_2 nodes.

Formation of PyC and SiO_2/PyC dual-phase nodes

PyC coatings and nodes were introduced via CVI using methane (CH_4) as the carbon source. The deposition was carried out at 1100 °C for 1–4 h under an 80 ml min^{-1} CH_4 flow rate. For samples requiring dual-phase nodes, the PyC layer was deposited onto pre-oxidized HC-SiC@SiO_2 NWAs, resulting in the formation of SiO_2/PyC dual-phase coatings and inter-nanowire nodes. For comparison, PyC-only samples were prepared by applying the same CVI treatment directly to unoxidized HC-SiC NWAs, forming HC-SiC@PyC NWAs. Specifically, the CVI time was set to 1 h for samples with a density of 50 mg cm^{-3}, 2 h for 100 mg cm^{-3}, and 4 h for 200 mg cm^{-3}. This adjustment was made to maintain a similar mass gain ratio across the samples.

Material characterization

SEM images were using a field emission scanning electron microscope (Quanta 600, FEI, United States) operated at an acceleration voltage of 5 kV. The microstructures of the nanowires were investigated using a field emission transmission electron microscope (JEM-F200, JEOL, Japan) equipped with EDS at an acceleration voltage of 200 kV. Compressive tests were carried out using a universal tester (EUT6104, Suns Co., Ltd., China) with a 10 kN load cell, and were applied a loading rate of 2 mm·min^{-1}. The samples for the compression testing were approximately 8 × 8 × 8 mm^3. Resilience at 80% is calculated based on the stress-strain curve with a maximum strain of 80%. It is defined as $100\% - \frac{\text{unrecoverablestrain}}{80\%}$, where the unrecoverable strain is determined from the unloading phase of the curve. The energy loss coefficient is calculated based on the stress–strain curves obtained under a compressive strain of 5%, using the following formula: Energy Loss Coefficient = $\frac{A_{\text{hysteresis}}}{A_{\text{loading}}}$ where $A_{\text{hysteresis}}$ is the area enclosed by the loading–unloading loop and A_{loading} is the area under the loading curve. The DMA was carried out using a Netzsch DMA 242E instrument. All mechanical tests were performed on three independent samples for each aerogel type to ensure statistical reliability ($n = 3$). The density of the aerogels was determined by dividing the measured mass by the corresponding geometric volume. The thermal conductivity of the samples was measured by the transient hot-wire method using a TC3000E thermal conductivity analyzer (XIATECH, China).

Computational simulations

MD simulations. In the LAMMPS simulations (version 3 Mar 2020), a SiC nanowire with a length of 78 Å and a diameter of 15 Å was modeled. The diameter of the hexagonal SiC nanowire was defined as the average of two radial distances: from the center to the corner and from the center to the edge. A 2.5 Å-thick amorphous SiO_2 coating was conformally deposited on the SiC surface, followed by a 9 Å-thick PyC layer. Bending deformation was introduced using a quasi-static displacement-controlled method. The nanowire model was partitioned into three regions along the *x*-axis: two fixed regions at both ends and a central free region. The atoms at the left and right ends were fully constrained to prevent rigid-body translation and rotation, while atoms in the central region were gradually displaced along the *y*-axis. A constant displacement rate of 0.02 Å/ps was applied to the central region with a time step of 1 fs, ensuring quasi-static loading conditions. For interatomic interactions, the Tersoff potential was used to describe Si–C and Si–Si interactions, as well as Si–O interactions within the SiO_2 region. The PyC layer was modeled using the AIREBO (Adaptive Intermolecular Reactive Empirical Bond Order) potential. Cross-interactions between chemically dissimilar atoms (e.g., C–O or Si–C between different phases) were excluded, and interfacial effects were approximated by nonbonded contact. All nanowire models were visualized using OVITO[29].

Finite element simulation. In the finite element modeling, a layered nanowire network was constructed within a simulation domain of 3 × 3 × 1.5 μm using SpaceClaim in combination with a Python API for geometry generation and preprocessing. A total of 1000 nanowires, each 2 μm in length, were randomly oriented in 3D space and converted from line segments into solid cylinders. To simulate coated nanowires, each SiC core was radially extruded to form a 14 nm thick SiO_2 layer, followed by an additional 14 nm PyC layer. The coatings were defined as perfectly bonded to the SiC core to represent ideal interfacial adhesion.

Inter-nanowire nodes were formed through controlled partial overlaps. Overlaps were retained only if the minimum distance between fibers fell within a threshold range of 114–120 nm; overlaps below this range were considered non-physical and removed to ensure structural integrity.

Compression–recovery simulations were performed by placing the nanowire assembly between two rigid planes. The bottom plane was fixed, while the top plane was constrained in the X and Y directions and applied a displacement load along the Z direction at a constant rate of 5 m/s. Contact between the top plane and the network was modeled using the automatic nodes to surface method, and fiber–fiber interactions were defined using contact automatic single surface option.

The mesh consisted of tetrahedral elements. The SiC@SiO_2@PyC model included 406,004 nodes and 1,338,255 elements; the SiC@SiO_2 and SiC@PyC models contained 300,158 nodes and 721,907 elements, respectively. The maximum compressive strain applied was 50%. Material properties used in the simulation are provided in Supplementary Table 3. To qualitatively capture damage evolution during compression, a maximum principal strain failure criterion was employed. Once the local strain in an element exceeded the material-specific failure strain threshold, the element was deleted from the simulation to represent fracture or node separation. The threshold values were set as 0.05 for the SiC core, 0.07 for the SiO_2 coating, and 0.10 for the PyC coating, as summarized in Supplementary Table 3. This approach enabled visualization of localized damage while avoiding artificial stress accumulation, and provided mechanistic insight into the structural stability of different node designs.

The model was built in the LS-DYNA module of ANSYS Workbench 2022 R1, solved using the LS-DYNA solver, and post-processed with LS-PrePost (version R12.0). All materials were defined as rate-independent and linear elastic, and no viscoelastic or plastic effects were included. To ensure computational feasibility, a relatively high loading rate of 5 m s^{-1} was applied, which may introduce dynamic artifacts. However, since failure was governed solely by a maximum principal strain criterion (with element deletion beyond defined thresholds), the simulations qualitatively reflect stress distribution and failure patterns under consistent loading conditions.

Reporting summary

Further information on research design is available in the Nature Portfolio Reporting Summary linked to this article.

Acknowledgements

The authors appreciate the foundation support from the National Natural Science Foundation of China (No. 92263204, 52302070, 52102076), the Shaanxi Provincial Key Research and Development Program (2024CY-GJHX-40), the Characteristic Development Guidance Funds for the Central Universities and the China Postdoctoral Science Foundation (2023M742756), and the Top Young Talents Program of Xi'an Jiaotong University, and the Fundamental Research Funds for the Central Universities. The authors would like to thank Yuanbin Qin at Xi'an Jiaotong University and Jiao Li at the Instrument Analysis Center of Xi'an Jiaotong University for their help in TEM characterization.

Author contributions

D.L., L.S., and H.W. conceived and designed the research. D.L. conducted materials preparation and mechanical tests. D.L. and L.S. wrote the paper. L.S. and H.W. supervised the research. L.Z., M.N., K.P., P.Z., X.W., Z.N., and S.J. discussed the results and analyzed the data.

Competing interests

The authors declare no competing interests.

Data availability

The data generated in this study are provided in the Supplementary Information and Source Data file. Source data are provided with this paper.

References

1. Guo, J. et al. Hypocrystalline ceramic aerogels for thermal insulation at extreme conditions. *Nature* **606**, 909–916 (2022).
2. Rewatkar, P. M. et al. Sturdy, monolithic SiC and Si_3N_4 aerogels from compressed polymer-cross-linked silica xerogel powders. *Chem. Mater.* **30**, 1635–1647 (2018).
3. Zhao, S. et al. Additive manufacturing of silica aerogels. *Nature* **584**, 387–392 (2020).
4. Su, L. et al. Highly stretchable, crack-insensitive and compressible ceramic aerogel. *ACS Nano* **15**, 18354–18362 (2021).
5. Leventis, N., Sadekar, A., Chandrasekaran, N. & Sotiriou-Leventis, C. Click synthesis of monolithic silicon carbide aerogels from polyacrylonitrile-coated 3D silica networks. *Chem. Mater.* **22**, 2790–2803 (2010).
6. Wang, J. et al. Ultra-high radial elastic aerogel fibers for thermal insulation textile. *Adv. Funct. Mater.* **35**, 2417873 (2024).
7. Su, L. et al. Engineering the mechanical properties of resilient ceramic aerogels. *J. Am. Ceram. Soc.* **107**, 1468–1480 (2024).
8. Si, Y., Wang, X., Dou, L., Yu, J. & Ding, B. Ultralight and fire-resistant ceramic nanofibrous aerogels with temperature-invariant superelasticity. *Sci. Adv.* **4**, eaas8925 (2018).
9. Cheng, X. et al. Way to a library of Ti-series oxide nanofiber sponges that are highly stretchable, compressible, and bendable. *Adv. Mater.* **36**, 2307690 (2024).
10. Li, L. et al. Large-scale assembly of isotropic nanofiber aerogels based on columnar-equiaxed crystal transition. *Nat. Commun.* **14**, 5410 (2023).
11. Li, L. et al. Nanograin–glass dual-phasic, elasto-flexible, fatigue-tolerant, and heat-insulating ceramic sponges at large scales. *Mater. Today* **54**, 72–82 (2022).
12. Liu, H. et al. Building-envelope-inspired, thermomechanically robust all-fiber ceramic meta-aerogel for temperature-controlled dominant infrared camouflage. *Adv. Mater.* **36**, 2313720 (2024).
13. Zong, D. et al. Gradient pore structured elastic ceramic nanofiber aerogels with cellulose nanonets for noise absorption. *Adv. Funct. Mater.* **33**, 2301870 (2023).
14. Su, L. et al. Strong yet flexible ceramic aerogel. *Nat. Commun.* **14**, 7057 (2023).
15. Li, M. et al. Resilient and antipuncturing Si_3N_4 nanofiber sponge. *Nano. Lett.* **23**, 1289–1297 (2023).
16. Cheng, X., Liu, Y.-T., Si, Y., Yu, J. & Ding, B. Direct synthesis of highly stretchable ceramic nanofibrous aerogels via 3D reaction electrospinning. *Nat. Commun.* **13**, 2637 (2022).
17. Xu, X. et al. Double-negative-index ceramic aerogels for thermal superinsulation. *Science* **363**, 723–727 (2019).
18. Su, L. et al. Anisotropic and hierarchical SiC@ SiO_2 nanowire aerogel with exceptional stiffness and stability for thermal superinsulation. *Sci. Adv.* **6**, eaay6689 (2020).
19. Zhang, X. et al. Ultrastrong, superelastic, and lamellar multiarch structured ZrO_2–Al_2O_3 nanofibrous aerogels with high-temperature resistance over 1300 °C. *ACS Nano* **14**, 15616–15625 (2020).
20. He, H. et al. Ultrastrong and multifunctional aerogels with hyperconnective network of composite polymeric nanofibers. *Nat. Commun.* **13**, 4242 (2022).
21. Stevenson, A. J. et al. Strong, tough and stiff bioinspired ceramics from brittle constituents. *Nat. Mater.* **13**, 508–514 (2014).
22. Wei, X., Zhu, Q., Qian, J., Lin, Y. & Shenoy, V. Response of biopolymer networks governed by the physical properties of cross-linking molecules. *Soft Matter* **12**, 2537–2541 (2016).
23. Lu, D. et al. Strong, superelastic and multifunctional SiC@ pyrolytic carbon nanofibers aerogels. *Carbon* **192**, 219–226 (2022).
24. Lu, D. et al. Lightweight and strong ceramic network with exceptional damage tolerance. *ACS Nano* **17**, 1166–1173 (2022).
25. Zhuang, L. et al. Highly cross-linked carbon tube aerogels with enhanced elasticity and fatigue resistance. *Nat. Commun.* **14**, 3178 (2023).
26. Chen, M., Wu, B., Zhou, L., Zhu, Y. & Wu, H. Micromechanical properties of pyrolytic carbon with interlayer crosslink. *Carbon* **159**, 549–560 (2020).
27. Zhang, X. et al. Theoretical strength and rubber-like behaviour in micro-sized pyrolytic carbon. *Nat. Nanotechnol.* **14**, 762–769 (2019).
28. Lu, D. et al. Scalable fabrication of resilient SiC nanowires aerogels with exceptional high-temperature stability. *ACS Appl. Mater. Interfaces* **11**, 45338–45344 (2019).
29. Stukowski, A. Visualization and analysis of atomistic simulation data with OVITO–the open visualization tool. *Modell. Simul. Mater. Sci. Eng.* **18**, 015012 (2010).
30. Li, G. et al. Boron nitride aerogels with super-flexibility ranging from liquid nitrogen temperature to 1000 °C. *Adv. Funct. Mater.* **29**, 1900188 (2019).
31. Su, L. et al. Ultralight, recoverable, and high-temperature-resistant SiC nanowire aerogel. *ACS Nano* **12**, 3103–3111 (2018).
32. Wu, F., Liu, Y., Si, Y., Yu, J. & Ding, B. Multiphase ceramic nanofibers with super-elasticity from– 196–1600 °C. *Nano Today* **44**, 101455 (2022).
33. Xu, Z., Zhang, Y., Li, P. & Gao, C. Strong, conductive, lightweight, neat graphene aerogel fibers with aligned pores. *ACS Nano* **6**, 7103–7113 (2012).

34. Li, C. et al. Superelastic and arbitrary-shaped graphene aerogels with sacrificial skeleton of melamine foam for varied applications. *Adv. Funct. Mater.* **28**, 1704674 (2018).
35. Peng, M. et al. 3D printing of ultralight biomimetic hierarchical graphene materials with exceptional stiffness and resilience. *Adv. Mater.* **31**, 1902930 (2019).
36. Yeo, S. J. et al. A plesiohedral cellular network of graphene bubbles for ultralight, strong, and superelastic materials. *Adv. Mater.* **30**, 1802997 (2018).
37. Wu, M. et al. Superelastic graphene aerogel-based metamaterials. *Nat. Commun.* **13**, 4561 (2022).
38. Wang, H. et al. Ultra-lightweight and highly adaptive all-carbon elastic conductors with stable electrical resistance. *Adv. Funct. Mater.* **27**, 1606220 (2017).
39. Yu, Z. L. et al. Superelastic hard carbon nanofiber aerogels. *Adv. Mater.* **31**, 1900651 (2019).
40. Chang, X. et al. Multiscale interpenetrated/interconnected network design confers all-carbon aerogels with unprecedented thermo-mechanical properties for thermal insulation under extreme environments. *Adv. Mater.* **36**, 2308519 (2024).
41. Ye, Z. et al. Crack-induced superelastic, strength-tunable carbon nanotube sponges. *Adv. Funct. Mater.* **33**, 2303475 (2023).
42. Deng, B. et al. Composite bending-dominated hollow nanolattices: a stiff, cyclable mechanical metamaterial. *Mater. Today* **21**, 467–474 (2018).
43. Meza, L. R., Das, S. & Greer, J. R. Strong, lightweight, and recoverable three-dimensional ceramic nanolattices. *Science* **345**, 1322–1326 (2014).
44. Yang, H. et al. Superplastic air-dryable graphene hydrogels for wet-press assembly of ultrastrong superelastic aerogels with infinite macroscale. *Adv. Funct. Mater.* **29**, 1901917 (2019).

Additional information

Supplementary information The online version contains supplementary material available at https://doi.org/10.1038/s41467-025-66339-x.

Correspondence and requests for materials should be addressed to Lei Su or Hongjie Wang.

Peer review information *Nature Communications* thanks Christophe Martin, Xiang Xu, and the other, anonymous, reviewer(s) for their contribution to the peer review of this work. A peer review file is available.